

Role of Magnetite, Rutile and H₂S in C-O-H Fluids' Speciation: Implications For Localized Reduction Zones in the Shallow Upper Mantle

Shubham Choudhary

Wadia Institute of Himalayan Geology

Souvik Das

The University of Texas at Arlington

Koushik Sen (✉ koushik.geol@gmail.com)

Wadia Institute of Himalayan Geology

Santosh Kumar

Kumaun University

Research Article

Keywords: Abiotic Hydrocarbon, Kerguelen Plume, Oxygen Fugacity, Hydrogen Sulfide, Pyroxenite, Raman spectroscopy

Posted Date: January 12th, 2022

DOI: <https://doi.org/10.21203/rs.3.rs-1227564/v1>

License: © ⓘ This work is licensed under a Creative Commons Attribution 4.0 International License. [Read Full License](#)

Abstract

Carbon (C) and sulfur (S) bearing volatiles in the mantle are important as they control processes like metasomatism and melting that ultimately influence Earth's geochemical cycle. Here we report rare shallow mantle fluid inclusions in a pyroxenite, associated with the Kerguelen Plume, from Northeast India. Optical microscopy and Raman spectroscopy reveal primary inclusions of hydrocarbon (CH) fluid and calcite in diopsidic clinopyroxene (Cpx) of this pyroxenite. Another Cpx from the same rock shows a rare occurrence of pseudo-secondary polyphase fluid inclusions of hydrogen sulfide (H₂S), carbon monoxide (CO), rutile and calcite. We infer that metasomatic interaction between silicates and C-O-H volatiles generated these fluids, which are trapped as inclusions. We further suggest two factors controlling carbon speciation in these fluids 1) exsolution of magnetite and diffusion of Ti from the Cpx to form rutile and 2) oxidation buffering due to presence of H₂S that prevented the formation of CH and formed CO instead. Our study explains the existence of significant reduction zones at localized scale in the oxidized shallow upper mantle.

Introduction

Dominant volatiles in the Earth's mantle belong to C-O-H-S group, which can either be fluid phases, or dissolved within silicate-melts and nominally-anhydrous (and non-carbon-bearing) phases in the form of defects, or as carbonate-rich liquids¹. Oxygen fugacity (fO_2) controls the proportions of multiple oxidation states of an element in minerals and fluids/volatiles², which in turn regulates the speciation of these volatiles in the ambient mantle³. Redox processes such as reduction of CO₂-rich fluids/melts can affect fO_2 of the mantle on a local scale⁴. Trivalent iron cation (Fe³⁺) can also buffer redox conditions locally in the mantle through carbon-iron redox coupling⁵. One of the most significant facets of understanding fluids and volatiles in the lithospheric mantle is to ascertain the conditions that generate abiogenic hydrocarbons at this depth. The occurrence of abiogenic hydrocarbon (CH) in the mantle could be attributed to the reduction of carbonates⁶⁻⁸ or sourced from deeper depths in the mantle^{9,10}. Various experimental studies have suggested that reduced C-O-H fluids such as CH can also be stable at shallower levels e.g., 1 GPa in the presence of relatively oxidized mineral such as magnetite^{11,6}. It is widely considered that oxidation of high valency cations may lower the oxygen fugacity, which in turn, can influence the speciation of C-O-H-S fluid phases in the mantle¹². Evidences of formation and occurrence of abiogenic CH in shallow mantle derived natural rocks are scarce because shallow upper mantle is believed to be dominated by CO₂-H₂O¹³⁻¹⁵. However, lighter abiogenic CH can also form by reduction of CO₂ and/or CO₂-H₂O fluids at upper mantle conditions^{16,17}.

Here we document C-O-H-S volatiles (CH, H₂S and CO), calcite and rutile as syngenetic inclusions in diopsidic clinopyroxenes of pyroxenites in ultramafic-alkaline-carbonatite complex (UACC) of Sung valley, NE India. This pyroxenite is sourced from the magma generated by low degree partial melting of carbonated peridotite (alkaline wehrlite) at > 2.5 GPa^{18,19}. We further provide evidence that the speciation of C-O-H fluid phases is dictated by oxygen fugacity (fO_2), which in turn is controlled by a) high valency cations of iron and titanium along with b) hydrogen sulfide (H₂S).

Geology Of The Area

The rocks of Ultramafic-alkaline-carbonatite complex (UACC) of Sung valley intrude the Shillong Plateau of Meghalaya in northeastern India (Fig. 1a). Formation of this UACC is ascribed to the Kerguelen plume²⁰⁻²², the plume tail of which is now present as a hot spot beneath the Kerguelen Islands in the Indian ocean²³. The emplacement age of Sung valley (UACC) is well established and geochronological data with different proxies comply with the range 101-115 Ma^{24,18,25}. The Shillong plateau, which is almost rectangular in shape, occurs as a horst like feature bounded by the E-W trending Dauki and Brahmaputra fault systems in the south and the north, respectively (Fig. 1a). Three other UACC complexes of Shillong plateau (Jasra, Samchampi, and Swangkre) are also emplaced within the Shillong plateau²⁶. The Sung Valley UACC comprises of ultramafic rocks including serpentinized peridotite, pyroxenite, and melilitolite along with alkaline rocks (ijolite and nepheline syenite) and carbonatites²⁷. Major part of the complex is covered by pyroxenite, serpentinized peridotite and ijolites, whereas other rock types constitute less than 5% of the exposed outcrops¹⁸. Serpentinized peridotite, which occupies the central part of the complex, is enclosed by pyroxenite and these rock units represent the oldest rocks of the complex (Fig. 1b). Ijolite occurs as a ring structure intruding the pyroxenites. Small intrusions of melilitolite and nepheline syenites as small dykes in serpentinized peridotite are present in the northwestern part of the complex. Carbonatites occur as small dykes, veins and oval shaped bodies as youngest member of the complex in southeastern part (Fig. 1b).

The dominant rock type of the complex is pyroxenite, which mostly occurs in direct contact with quartzite of Shillong Group. Petrography and geochemistry of the Sung valley UACC have carried out by various workers in the past^{28,18,19}. Petrographic features of most pyroxenites include hypidiomorphic texture with medium to coarse grain size and ample amount of clinopyroxene, mainly- diopside with minor augite. The pyroxenites of Sung valley generally show greenish black to black color and consist dominantly of diopside with minor augite. Sung valley pyroxenites are nearly monomineralic as they show presence of ~95% clinopyroxenes (Cpx). Pyroxenites and other silicate rocks of Sung valley show inverse relationship between SiO₂-TiO₂ on Harker variation diagrams, where TiO₂ decreases with increasing SiO₂. However these silicate rocks do not show any definite co-genetic relationship¹⁸. It is well established that these rocks have derived from a primary magma, which was generated by partial melting of carbonated peridotite (alkaline wehrlite) at pressures greater than ~25 kbar^{18,19}.

Results

The studied pyroxenite (sample no. Px-9/3) consists of clinopyroxene (Cpx), dominantly diopside, with minor amount of augite (Figs. 1c, d). It shows cumulate texture (Fig. 2a). We categorized these cumulates into two petrographic varieties. Cumulate 1 show resorbed grain boundaries and one of these cumulates also hosts two sets exsolution lamellae of magnetite (Fig. 2b) whereas, cumulate 2 are relatively smaller with no signature of resorption. Modal content of Cpx is 75-85%. Accessory minerals of this pyroxenite include phlogopite, apatite and oxides (magnetite and ilmenite) (Fig. 2). Sulfides (mainly chalcopyrite) are present as globular curved trail of mineral inclusions within cumulate Cpx and in interstitial spaces (Figs. 2c, d). Modal abundance of accessory sulfide is <5% (Figs. 2c, d).

One of the diopsides (cumulate 1 Cpx) hosts a cluster of monophase primary fluid inclusions of hydrocarbon (CH) and solid inclusions of calcite within the core part (Fig. 3a). The two sets exsolution lamellae of magnetite are oriented nearly at right angle and concentrate in the core part of cumulate 1 Cpx (Fig. 2b). This textural feature suggests that magnetites are formed as primary exsolved phases (in different planes). The modal percent of magnetite exsolutions is ~ 4% (Fig. 2b). Another diopside cumulate (cumulate 2 Cpx) hosts an intragranular trail of polyphase fluid inclusions (Fig. 4a). The termination of this polyphase fluid inclusion trail within the host in cumulate 2 Cpx suggests that these fluid inclusions are pseudo-secondary in nature. Intragranular trail of these fluid inclusions indicates that the entrapment of fluids took place in a fracture that developed and healed during the continued growth of the cumulate 2 Cpx crystal²⁹ (Fig. 4a). High phase ratio of solid to liquid and gas can be clearly observed in polyphase fluid inclusions hosted by cumulate 2 Cpx, as these inclusions show granular appearance (Fig. 4a). Inclusions in cumulate 1 Cpx range from 4-6 μm (Fig. 3a) and in cumulate 2 Cpx from 5-12 μm (Fig. 4a) in size. Petrographic features such as the occurrence of monophase inclusions in the core of cumulate 1 Cpx and termination of polyphase inclusion trail prior to cumulate 2 Cpx boundary suggest that these fluid inclusions were trapped during the growth of these crystals²⁹.

Raman spectrum obtained from cumulate 1 shows the host as diopside with two strong bands at 667 and 1012 cm^{-1} (Fig. 3c), where the 667 cm^{-1} Raman band being characteristic of clinopyroxene silicate chain³⁰. Monophase inclusions were identified as lighter abiotic hydrocarbon (CH) fluid, showing antisymmetric bands at 2906 cm^{-1} and 2969 cm^{-1} in high frequency region (Fig. 3c1)^{31, 6, 32} and calcite showing its symmetric stretching vibration band at 1088 cm^{-1} and strong vibration band at 286 cm^{-1} (Fig. 3d, d1)³³. In the Raman spectrum of CH (Fig. 3c1) a three-component band (maxima at 2906, 2895 and 2913 cm^{-1}) was observed. Two shoulder peaks at 2895 and 2913 cm^{-1} give this band a broader appearance and these peaks correspond to ethane and methane respectively³². The second three component band with maxima at 2969 cm^{-1} marks the presence of propane with characteristic signature of methyl group^{32, 34}. Many of these monophase inclusions (Fig. 3a) were analyzed by Raman spectroscopy repeatedly and they are either entirely CH fluid or calcite. The exsolution needles hosted by cumulate 1 Cpx were identified as magnetite with Raman spectroscopy and the spectrum obtained shows strong band at 542 cm^{-1} and very strong band at 666 cm^{-1} (Fig. 3b, b1)³³.

In the present study, absence of CH peaks in the other spectra e.g., of magnetite exsolutions (Fig. 3b) and calcite inclusions (Fig. 3d) around 3000 cm^{-1} , rules out the possibility of abiotic CH spectrum to be sourced from epoxy used during the sample preparation. Besides epoxy used during the sample preparation (spectrum acquired separately) shows bands at different shifts (1432, 2880 and 3066 cm^{-1}) with totally different spectral signatures (Supplementary materials Fig. 1).

Raman spectra of fluid inclusions in cumulate 2 Cpx (Fig. 4a) show the host as diopside with two strong bands at 664 and 1010 cm^{-1} (Fig. 4c). Polyphase fluid inclusions in the pseudo-secondary inclusion trail (Fig. 4a) were identified as volatile phases of hydrogen sulfide (H_2S), showing its ν_3 vibration at 2628 cm^{-1} (Fig. 4c1)³⁵ and carbon monoxide (CO) showing its main vibration at 2147 cm^{-1} (Figs. 4d, d1)³⁶. Solid phase rutile is detected with very strong (vs) vibrations at 447 cm^{-1} and 609 cm^{-1} (Figs. 4b, b1) and calcite with symmetric stretching vibration band at 1085 cm^{-1} and strong bands at 282 cm^{-1} (Fig. 4b)³⁴. Electron Microprobe (EPMA) analysis confirms that all Cpx are diopside (Fig. 5a) and cumulate 2 Cpx grains have a higher amount of TiO_2 as compared to the cumulate 1 Cpx (Table 1). These cumulate Cpx display almost jadeite-free composition (Fig. 5b). We obtained a P - T range of pyroxenite crystallization of ~1.5 - 1.9 GPa and 717°C to 1128°C respectively through single-clinopyroxene geothermobarometric analysis by Winpyrox program (Table 2)³⁷. Oxygen fugacity ($f\text{O}_2$) was constrained using thermodynamic calculations of the pyroxenite (Px-9/3) in the $\text{CaO-TiO}_2\text{-FeO-O}_2\text{-CO}_2$ system at 900°C, (similar to Tao et al. 2018, 2020)^{7,8} using Perplex 6.7.8 (versions June 6th 2017)³⁸ and internally consistent thermodynamic dataset³⁹ (Figs. 5c, d). The pressure range and sectioning value for temperature given during the calculations were according to the P - T obtained through geothermobarometry (Table 2). The oxygen fugacity was constrained in the range between -7 to -9 log units (Figs. 5c, d), using solution model for carbonate⁴⁰ where assemblage of calcite, rutile and magnetite is stable.

Table 1

Quantitative mineral chemistry data. Table showing composition of diopsides (cumulate 1 and cumulate 2) based on EPMA point analysis.

Sample Px-9/3	Clinopyroxene-Cumulate 1					Clinopyroxene-Cumulate 2									
	(cr= core; rm= rim) (spot 1 to 5)					(cr= core; rm= rim) (spot 6 to 15)									
Spot analysis	1	2	3	4	5	6	7	8	9	10	11	12	13	14	15
	cr	cr	cr	rm	rm	cr	rm	cr	rm	cr	rm	cr	rm	cr	rm
SiO ₂	51.6	51.88	52.17	51.18	52.28	52.27	52.68	51.81	51.23	50.75	50.54	53.49	52.98	50.75	51.93
TiO ₂	0.64	0.55	0.5	0.62	0.64	0.56	0.58	1.02	0.79	0.9	1.12	0.48	0.78	1.03	0.88
Al ₂ O ₃	2.12	1.92	1.91	2.25	2.34	1.88	1.95	3.23	2.43	2.94	3.36	1.44	2.52	3.19	2.87
Cr ₂ O ₃	0.21	0.2	0.2	0.22	0.18	0.31	0.35	0.02	0.06	0.06	0.04	0.13	0.05	0.04	0.09
Fe ₂ O ₃	1.33	1.44	1.28	2.63	1.85	2.49	2	2.56	2.12	2.2	3.16	0.59	1.14	2.39	2.75
FeO	2.67	2.56	2.48	1.37	2.43	1.72	2.18	2.3	2.45	2.49	1.73	3.01	2.97	2.66	2.01
MnO	0.15	0.08	0.18	0.17	0.19	0.15	0.12	0	0	0.05	0.06	0.17	0.36	0.03	0.21
MgO	14.66	15.02	14.89	14.72	14.89	15.4	15.07	14.76	14.58	14.52	14.55	15.72	15.33	14.46	15.02
CaO	24.53	24.63	25.06	24.85	24.86	24.67	25.15	25.43	24.98	24.49	24.9	24.75	24.66	24.54	25.08
Na ₂ O	0.41	0.34	0.33	0.45	0.45	0.45	0.45	0.36	0.31	0.37	0.38	0.32	0.35	0.37	0.37
K ₂ O	0	0	0	0.02	0	0	0.02	0.01	0.03	0	0.02	0	0.05	0	0.02
Total	98.33	98.61	98.99	98.48	100.12	99.91	100.54	101.5	98.99	98.76	99.86	100.11	101.2	99.44	101.23
On the basis of 60															
Si	1.928	1.932	1.935	1.91	1.919	1.921	1.926	1.881	1.906	1.892	1.865	1.957	1.922	1.881	1.889
Ti	0.018	0.015	0.014	0.018	0.018	0.015	0.016	0.028	0.022	0.025	0.031	0.013	0.021	0.029	0.024
Al	0.094	0.084	0.084	0.099	0.101	0.082	0.084	0.138	0.107	0.129	0.146	0.062	0.108	0.14	0.123
Cr	0.006	0.006	0.006	0.007	0.005	0.009	0.01	0.001	0.002	0.002	0.001	0.004	0.001	0.001	0.003
Fe ³	0.038	0.04	0.036	0.074	0.051	0.069	0.055	0.07	0.059	0.062	0.088	0.016	0.031	0.067	0.075
Fe ²	0.084	0.08	0.077	0.043	0.075	0.053	0.067	0.07	0.076	0.078	0.054	0.092	0.09	0.082	0.061
Mn	0.005	0.002	0.006	0.005	0.006	0.005	0.004	0	0	0.002	0.002	0.005	0.011	0.001	0.006
Mg	0.817	0.833	0.823	0.819	0.814	0.843	0.821	0.798	0.809	0.807	0.8	0.857	0.829	0.799	0.814
Ca	0.982	0.983	0.996	0.993	0.978	0.971	0.985	0.989	0.996	0.978	0.985	0.97	0.959	0.975	0.977
Na	0.03	0.024	0.024	0.032	0.032	0.032	0.032	0.025	0.022	0.026	0.027	0.023	0.025	0.027	0.026
K	0	0	0	0.001	0	0	0.001	0.001	0.001	0	0.001	0	0.003	0	0.001
Total	4	4	4	4	4	4	4	4	4	4	4	4	4	4	4
Mg#	90.67	91.23	91.44	95.01	91.56	94.08	93.74	91.93	91.41	91.18	93.6	90.30	90.20	90.69	93.02

Table 2
Geothermobarometry data. Table showing mineral chemistry data involved in the P - T calculations by Winpyrox program (Yavuz, 2013).

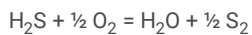
Representative points no. of Cpx chemistry (data is already shown in Table 1)	Pressure (GPa)	Temperature T (°C)
1 cr Cpx 1	1.9	910
2 cr Cpx 1	1.8	793
3 cr Cpx 1	1.8	862
4 rm Cpx 1	1.6	723
5 rm Cpx 1	1.9	911
6 cr Cpx 2	1.6	791
7 rm Cpx 2	1.7	864
8 cr Cpx 2	1.8	814
9 rm Cpx 2	1.8	717
10 cr Cpx 2	1.6	909
11 rm Cpx 2	0.8	912
12 cr Cpx 2	1.6	973
13 rm Cpx 2	1.8	1128
14 cr Cpx 2	1.5	1028
15 rm Cpx 2	1.7	1000

Discussion

The fluids and volatiles in the mantle are sourced from both recycled crust and primitive mantle⁴¹. Past studies have shown that oceanic crust (rich in carbonate) can subduct as deep as the lower mantle depths⁴² and it can also be recycled into the mantle plumes⁴³. Solubility of sulfur in mantle magma is controlled by oxygen and sulfur fugacities (fO_2 and fS_2) and FeO concentration⁴⁴. Occurrence of sulfides in mantle derived rocks suggests that there is a significant concentration of sulfur and chalcophile elements in the mantle (subducted through oceanic crust and sediments⁴⁵. Sulfide phases (chalcopyrite) present as inclusions in Cpx as well as accessory phases in these pyroxenites (Figs. 2c, d) along with the fluid inclusions of H_2S in cumulate 2 Cpx (Fig. 4c) indicate that the parental diopsidic magma of pyroxenite was saturated with sulfur as a result of decreasing sulfur solubility in silicate melt during decompression.

Association of CH and calcite can be explained through different mechanisms at different depths in the mantle. Many experimental as well as natural evidences have shown the formation of CH through reduction of carbonates (calcite in the present case). They suggest that when carbonates are exposed to mantle pressures and temperatures under reducing conditions, they can be broken down to CH in Earth's mantle⁶⁻⁸. However, this possibility can be ruled out in the present scenario as hydrocarbon formation through the reduction of carbonates in the above-mentioned studies were documented mostly at higher pressures e.g., 3-11 GPa and our P - T calculations suggest the crystallization of this pyroxenite at ~ 1.5 to 1.9 GPa (Table 2). Furthermore, jadeite-free compositions of the analyzed Cpx in the present study (Fig. 5b; Table 1) and absence of any high pressure polymorph of these Cpx again substantiate our inference that this pyroxenite was crystallized at shallower depth in shallow upper mantle (Fig. 6). Even if the possible breakdown of carbonate to CH took place at the time of generation of primary silicate magma, from a metasomatized carbonated peridotite at a pressure greater than ~ 2.5 GPa¹⁸, it is highly unlikely that the CH formed in such a way will not be reequilibrated during its ascent from >2.5 GPa (base of the lithospheric mantle) to crystallization at 1.5-1.9 GPa (even shallower upper mantle). The Sung valley pyroxenite is a product of magma generated by low degree partial melting of carbonated peridotite (alkaline wehrlite)^{18,19}, hence, activity of CO_2 - H_2O -bearing carbonate-rich metasomatic fluids cannot be ignored. These CO_2 - H_2O -bearing fluids show high mobility in the mantle and potentially can give rise to carbonates through the reaction with mafic silicate minerals in the lithospheric mantle⁴⁶. We envisage that this CO_2 - H_2O bearing metasomatic fluid interacted with Ca-rich diopsidic magma to form calcite (Fig. 3d). Simultaneously, as magnetite exsolved from the diopside (Fig. 2b), the prevailing fO_2 remained low. H_2O dissociated to produce oxygen for magnetite and excess hydrogen (H) reduced remaining CO_2 - H_2O bearing fluid (redox sensitive C-O-H fluid) to CH fluid (Fig. 3c, c1). Although dissociation of H_2O to H_2 and O_2 at shallow upper mantle is low⁴⁷, but fO_2 lowered by the exsolution of magnetite would increase the degree of dissociation of H_2O . We infer that dissociation of H_2O can drive this redox reaction to give rise to these micron scale inclusions of fluid CH and calcite (Fig. 3a). Fluid CH and calcite were trapped in the host as primary inclusions during the crystallization of cumulate 1 Cpx (Fig. 6). The presence of magnetite strongly favors these reducing conditions to prevail even at shallower mantle depth up to ~ 1 GPa pressure^{11,6}. The presence of excess water, if any can be explained by the formation of phlogopite (Fig. 2a).

Formation of calcite in the polyphase fluid inclusions in the cumulate 2 Cpx can be explained similar to that of cumulate 1 Cpx. Calcite detected in cumulate 2 Cpx is also formed by the reaction between redox sensitive CO₂-H₂O-bearing fluids with crystallizing host diopside⁴⁸. It is interesting to note that the presence of rutile in these inclusions displays a redox couple between titanium and carbon/oxygen. We infer that tetravalent titanium cation (Ti⁴⁺) from the host diopside (cumulate 2 Cpx; which shows quite high Ti content; Table 1) diffused into the fluid inclusion to form rutile⁴⁹. Formation of rutile also kept the prevailing *f*O₂ low. Simultaneously H₂O dissociated to produce the oxygen for rutile and the excess hydrogen (H) reduced these CO₂-H₂O-bearing fluids to CO and H₂S. The redox processes in this study support the existence of reduction zones in oxidized shallow upper mantle⁴ probably on a local scale. Fluid CO, H₂S and calcite, rutile were trapped in the host diopside as pseudo-secondary inclusions along the healed fracture during the crystallization of cumulate 2 Cpx (Fig. 6). Detected rutile and calcite in cumulate 2 Cpx could possibly be daughter crystals formed upon the reaction of CO₂-H₂O fluids with diopside after its crystallization. However, this possibility is low because reduction of CO₂-H₂O fluid to CO and H₂S is not possible after entrapment since sulfur can only be incorporated in these inclusions from parental melt before the entrapment of these fluids. As discussed earlier, it is evident that the parental magma of pyroxenite was saturated with sulfur (S) and the presence of S can be explained by the decrease in its solubility in silicate melt during decompression. Since the *f*O₂ and *f*S₂ are inversely proportional⁵⁰, decreased solubility of S in the silicate melt further lowers *f*O₂ as *f*S₂ increases. It is observed that in cumulate 2 Cpx, despite such reducing environment, CO was formed in the fluid inclusions instead of CH (Fig. 4d1). Since very low *f*O₂ is prevented by redox buffering caused by H₂S, which controls the formation of reduced carbon phases like CH⁵¹. Therefore, it can be inferred that in the present study, only CO was detected in these fluid inclusions instead of CH in cumulate 2 Cpx due to the redox buffering caused by H₂S through the following redox reaction



Conclusions

We conclude that redox sensitive metasomatic C-O-H fluids can also give rise to abiotic CH in the shallower upper mantle due to reducing conditions triggered by Fe³⁺ and Ti⁴⁺ cations in magnetite and rutile respectively.

The solid inclusions (calcite and rutile) in the cumulate Cpx are evidently formed through the reaction of C-O-H fluids with crystallizing host diopside (Fig. 6).

The fluids CO and H₂S are speciated varieties of CO₂-H₂O (C-O-H) fluids, where speciation was controlled by changing (*f*O₂).

Analytical Methods

Electron Probe Micro Analyses (EPMA):

Thin sections were prepared for petrographic and electron microprobe analyses. EPMA data acquisition was carried out at the Department of Geology, Institute of Science, Banaras Hindu University, using a CAMECA SXFiveSA Electron Probe Micro Analyzer equipped with a Wavelength dispersive spectrometry and a LaB6 source was used to carry out quantitative analyses. Analytical conditions employed for quantitative analysis of silicates (especially Cpx) were, acceleration voltage 25 kV and beam current of 10 nA having diameter of 1 μm. The standards which were used for calibration were natural minerals including diopside, peridot, almandine, albite and orthoclase. For quantitative measurements TAP (thallium acid phthalate), LPET (large pentaerythritol) and LLIF (large lithium fluoride) crystals were used. The precision of analyses for major oxides were less than 1%. Mineral chemistry data for the studied sample is given in Table 1.

Raman Spectroscopy:

Micro Raman spectroscopy was carried out with a Thermo Scientific DXRxi Raman imaging spectroscope in the Department of Earth and Environmental Science, University of Texas at Arlington, USA. All the Raman spectra and mapping were generated using 10X and 50X objectives and with the 532 nm laser with a dispersion of a fixed holographic grating 900 lines/mm. The laser spot size at the time of analyses were ~ 2 μm. Repeated spectra were recorded in the 100-4000 cm⁻¹ region for a better signal to noise ratio. During Raman analysis other parameters were taken as follows- acquisition time ~ 1 – 5 sec, accumulations ~ 1 – 5 and laser power ~ 2 – 6 mW. During Raman mapping, laser power was 3.0 mW and image pixel size was 1 μm. The pinhole was kept at 25 μm during all these analyses. Preparation of Raman maps was done in standard 2D mode along the XY plane of the thin section. General consideration of accuracy of Raman peak was ± 1 cm⁻¹ to obtain better and accurate data. RGB (Red-Green-Blue) color mode was chosen at the time of Raman mapping. Calibration of the DXRxi Raman imaging microscope was done through auto-alignment and Si (520.5 cm⁻¹ peak).

X-Ray Fluorescence:

Major-oxides of the studied sample (Px-9/3) from Sung valley pyroxenites were measured by wavelength dispersive X-ray fluorescence (Siemens SRS 3000) on pressed pellet at the Wadia Institute of Himalayan Geology (WIHG). Crushing and pulverizing was done using an agate carbide ring grinder, and 7 g aliquots of rock powder were used to make pressed pellet for the sample. Analytical precision for major elements was observed ±2-3%. International reference samples GA, GH, GSN, MA-N (CRPG France), G-2, GSP-1, RGM-1, AGV-1 (USGS, USA), and JG-2, JG1-a, and JA-2 (GSJ, Japan) were used to check precision and accuracy of the preparation and instrumental performances. Calibration coefficients were driven using a modified model with intensity-based matrix correction⁵².

Declarations

Acknowledgements

Director, WIHG is thanked for his encouragement and support. A. R. Basu, University of Texas at Arlington, USA, is thanked for providing Raman spectroscopic facility. N. V. C. Rao and D. Pandit, Banaras Hindu University are thanked for microprobe analyses. This work is part of doctoral research work of SC.

Author contributions

Conceptualization: All authors; Data curation: SC, SD and KS; Investigation: SC and KS; Methodology: SC and SD; Statistical analysis and figure generation: SC and SD; Writing—original draft: SC; Writing—review and editing: KS and SK; Supervision and advice: KS and SK; Funding arrangement: KS.

Funding

This research did not receive any specific grant from funding agencies in the public, commercial, or not-for-profit sectors.

References

1. Frezzotti, M. L. & Peccerillo, A. Diamond-bearing COHS fluids in the mantle beneath Hawaii. *Earth Planet. Sci. Lett.* **262**, 273–283 (2007).
2. Stagno, V. & Fei, Y. The redox boundaries of earth's interior. *Elements: An International Magazine of Mineralogy, Geochem. Petrol.* **16**(3), 167–172 (2020).
3. Stagno, V., Ojwang, D. O., McCammon, C. A. & Frost D. J. The oxidation state of the mantle and the extraction of carbon from Earth's interior. *Nature.* **493**(7430), 84–88 (2013).
4. Frost, D. J. & McCammon, C. A. The Redox State of Earth's Mantle. *Annu. Rev. Earth Planet. Sci.* **36**, 389–420 (2008).
5. Rohrbach, A. & Schmidt M. W. (2011) Redox freezing and melting in the Earth's deep mantle resulting from carbon–iron redox coupling. *Nature.* **472**(7342), 209–212.
6. Scott, H. P. *et al.* Generation of methane in the Earth's mantle: in situ high pressure–temperature measurements of carbonate reduction. *Proc. Natl. Acad. Sci. U. S. A.* **101**, 14023–14026 (2004).
7. Tao, R. *et al.* Formation of abiogenic hydrocarbon from reduction of carbonate in subduction zones: Constraints from petrological observation and experimental simulation. *Geochim. Cosmochim. Ac.* **239**, 390–408 (2018).
8. Tao, R., Zhang, L. & Zhang, L. Redox evolution of western Tianshan subduction zone and its effect on deep carbon cycle. *Geosci. Front.* **11**(3), 915–924 (2020).
9. Palot, M., Cartigny, P., Harris, J. W., Kaminsky, F. V. & Stachel, T. Evidence for deep mantle convection and primordial heterogeneity from nitrogen and carbon stable isotopes in diamond. *Earth Planet. Sci. Lett.* **357**, 179–193 (2012).
10. Das, S., Basu, A. R. & Mukherjee, B. K. In situ peridotitic diamond in Indus ophiolite sourced from hydrocarbon fluids in the mantle transition zone. *Geology.* **45**, 755–758 (2017).
11. Xiao, W. S., Chai, P. X., Wang, B. S. & Weng, K. N. Hydrocarbon formation by reactions of graphite with water-containing minerals under high pressure and high temperature. *Prog. Nat. Sci.* **9**, 395–398 (1999).
12. McCammon, C. The paradox of mantle redox. *Science.* **308**, 807–808 (2005).
13. Roedder, E. Fluid inclusions, Reviews in mineralogy. *Min. Soc. America.* **12**, 644 (1984).
14. Bucher-Nurminen, K. Transfer of mantle fluids to the lower continental crust: Constraints from mantle mineralogy and Moho temperature. *Chem. Geol.* **83**(3–4), 249–261 (1990).
15. Wyllie, P. J. & Ryabchikov, I. D. Volatile components, magmas, and critical fluids in upwelling mantle. *J. Petrol.* **41**(7), 1195–1206 (2000).
16. Sokol, A. G., Tomilenko, A. A., Bul'bak, T. A. & Sobolev, N. V. Synthesis of hydrocarbons by CO₂ fluid conversion with hydrogen: Experimental modeling at 7.8 GPa and 1350° C. *Dokl. Earth Sci.* **477** (2), 1483–1487 (2017).
17. Sokol, A., Tomilenko, A., Sokol, I., Zaikin, P. & Bul'bak, T. Formation of hydrocarbons in the presence of native iron under upper mantle conditions: Experimental constraints. *Minerals.* **10**(2), 88 (2020).
18. Srivastava, R. K. & Sinha A. K. Early Cretaceous Sung Valley ultramafic-alkaline-carbonatite complex, Shillong Plateau, Northeastern India: petrological and genetic significance. *Min. Petrol.* **80**, 241–263 (2004).
19. Srivastava, R. K., Heaman, L. M., Sinha, A. K. & Shihua, S. Emplacement age and isotope geochemistry of Sung Valley alkaline–carbonatite complex, Shillong Plateau, northeastern India: implications for primary carbonate melt and genesis of the associated silicate rocks. *Lithos.* **81**, 33–54 (2005).
20. Veena, K., Pandey, B. K., Krishnamurthy, P. & Gupta, J. N. Pb, Sr and Nd Isotopic Systematics of the Carbonatites of Sung Valley, Meghalaya, Northeast India: Implications for Contemporary Plume-Related Mantle Source Characteristics. *J. Petrol.* **39**, 1875–1884 (1998).
21. Ray, J. S., Ramesh, R. & Pande, K. Carbon isotopes in Kerguelen plume-derived carbonatites: evidence for recycled inorganic carbon. *Earth. Planet. Sci. Lett.* **170**, 205–214 (1999).

22. Ray, J. S., Trivedi, J. R. & Dayal, A. M. Strontium isotope systematics of Amba Dongar and Sung Valley carbonatite-alkaline complexes, India: evidence for liquid immiscibility, crustal contamination and long-lived Rb/Sr enriched mantle sources. *J. Asian Earth Sci.* **18**, 585–594 (2000).
23. Storey, M., *et al.* Lower Cretaceous vol-canic rocks on continental margin and their relationship to Kerguelen Plateau. *Proc. Ocean Drill. Prog. Sci. Results.* **120**, 33-54 (1992).
24. Ray, J. S. & Pande, K. ⁴⁰Ar-³⁹Ar age of carbonatite-alkaline magmatism in Sung valley, Meghalaya, India. *J. Asian Earth Sci.* **110**, 185–190 (2001).
25. Srivastava, R. K., Guarino, V., Wu, F. Y., Melluso, L. & Sinha, A. K. Evidence of sub-continental lithospheric mantle sources and open-system crystallization processes from in-situ U–Pb ages and Nd–Sr–Hf isotope geochemistry of the Cretaceous ultramafic-alkaline (carbonatite) intrusions from the Shillong Plateau, north-eastern India. *Lithos.* **330**, 108–119 (2019).
26. Srivastava, R. K. & Sinha, A. K. Geochemistry of Early Cretaceous alkaline ultramafic-mafic complex from Jasra, Karbi Anglong, Shillong plateau, northeastern India. *Gondwana Res.* **7**, 549–561 (2003).
27. Yusuf, S. & Saraswat, A.C. A preliminary note on carbonatite in the Sung Valley of Jaintia Hills district, Meghalaya: *Curr. Sci.* **46**, 703–704 (1977).
28. Melluso, L., Srivastava, R. K., Guarino, V., Zanetti, A. & Sinha, A. K. Mineral Compositions and Petrogenetic Evolution of the ultramafic-alkaline-carbonatite complex of Sung valley, Northeastern India. *Canad. Mineral.* **48**, 205–229 (2010).
29. Roedder, E. Fluid inclusions as samples of ore fluids. *Geochemistry of hydrothermal ore deposits* (1979).
30. Thompson, J., Wiens, R., Sharma, S., Lucey, P. & Misra, A. Combined remote LIBS and Raman spectroscopy measurements. *Lunar and Planetary Science XXXVI* pdf., 1517 (2005).
31. Zhang, N., Tian, Z., Leng, Y., Wang, H., Song, F. & Meng, J. Raman characteristics of hydrocarbon and hydrocarbon inclusions. *Sci. China Earth Sci.* **50**, 1171–1178 (2007).
32. Atamas, N. A., *et al.* A study of the Raman spectra of alkanes in the Fermi-resonance region. *J. Mol. Struct.* **708**, 189–195 (2004).
33. Frezzotti, M. L., Tecce, F. & Casagli, A. Raman spectroscopy for fluid inclusion analysis. *J. Geochem. Explor.* **112**, 1–20 (2012).
34. Frezzotti, M. L. Diamond growth from organic compounds in hydrous fluids deep within the Earth. *Nat. Commun.* **10**, 1–8 (2019).
35. Tang, S. Y. & Brown, C. W. Raman spectrum of matrix isolated hydrogen sulphide. *J. Raman Spectrosc.* **2**, 209–215 (1974).
36. Burke, E. A. J. Raman microspectrometry of fluid inclusions. *Lithos.* **55**, 139–158 (2001).
37. Yavuz, F. WinPyrox: a Windows program for pyroxene calculation classification and thermobarometry. *Am. Mineral.* **98**, 1338–1359 (2013).
38. Connolly, J. A. D. The geodynamic equation of state: What and how. *Geochem Geophys.* **10**(10) (2009). doi:10.1029/2009GC002540.
39. Holland, T. I. M. & Powell, R. Calculation of Phase Relations Involving Haplogranitic Melts Using an Internally Consistent Thermodynamic Dataset. *J. Petrol.* **42**(4), 673–683 (2001).
40. Anovitz, L. M. & Essene, E. J. Phase equilibria in the system CaCO₃-MgCO₃-FeCO₃. *J. Petrol.* **28**(2), 389–415 (1987).
41. Timmerman, S., *et al.* Primordial and recycled helium isotope signatures in the mantle transition zone. *Science.* **365**(6454), 692–694 (2019).
42. Nestola F., *et al.* CaSiO₃ perovskite in diamond indicates the recycling of oceanic crust into the lower mantle. *Nature.* **555**, 237–241 (2018).
43. Huang, S. & Frey, F. A. Recycled oceanic crust in the Hawaiian Plume: evidence from temporal geochemical variations within the Koolau Shield. *Contrib. Mineral. Petr.* **149**, 556–575 (2005).
44. Haughton, D. R., Roeder, P. L. & Skinner B. J. Solubility of sulphur in mafic magmas. *Econ. Geol.* **69**, 451–467 (1974).
45. Ding, S. & Dasgupta, R. Sulphur inventory of ocean island basalt source regions constrained by modeling the fate of sulphide during decompression melting of a heterogeneous mantle. *J. Petrol.* **59**, 1281–1308 (2018).
46. Choudhary, S., Sen, K., Kumar, S., Rana, S. & Ghosh, S. Forsterite reprecipitation and carbon dioxide entrapment in the lithospheric mantle during its interaction with carbonatitic melt: a case study from the Sung Valley ultramafic–alkaline–carbonatite complex, Meghalaya, NE India. *Geol. Mag.* **1–12** (2020).
47. Frost, B. R. & Ballhaus C. Comment on " Constraints on the origin of the oxidation state of mantle overlying subduction zones: an example from Simcoe, Washington, USA" by AD Brandon and DS Draper. *Geochim. Cosmochim. Ac.* **62**, 329–332 (1998).
48. Andersen, T., O'Reilly, S. Y. & Griffin, W.L. The trapped fluid phase in upper mantle xenoliths from Victoria, Australia: implications for mantle metasomatism. *Contrib. Mineral. Petr.* **88**, 72–85 (1984).
49. Larsen, R. B., Eide, E. A. & Burke, E. A. Evolution of metamorphic volatiles during exhumation of microdiamond-bearing granulites in the Western Gneiss Region, Norway. *Contrib. Mineral. Petr.* **133**(1-2), 106–121 (1998).
50. Kiseeva E. S., Fonseca R. O. and Smythe D. J. (2017) Chalcophile elements and sulfides in the upper mantle. *Elements.* **13**(2), 111–116.
51. Bény, C., Guilhaumou, N. & Touray, J. C. Native-sulphur-bearing fluid inclusions in the CO₂-H₂S-H₂O-S system—Microthermometry and Raman microprobe (MOLE) analysis—Thermochemical interpretations. *Chem. Geol.* **37**, 113–127 (1982).
52. Lucas-Tooth, H. J. & Pyne, C. The accurate determination of major constituents by X-ray fluorescence analysis in the presence of large interelement effects. *Adv. X-Ray Anal.* **7**, 523–541 (1964).

Figures

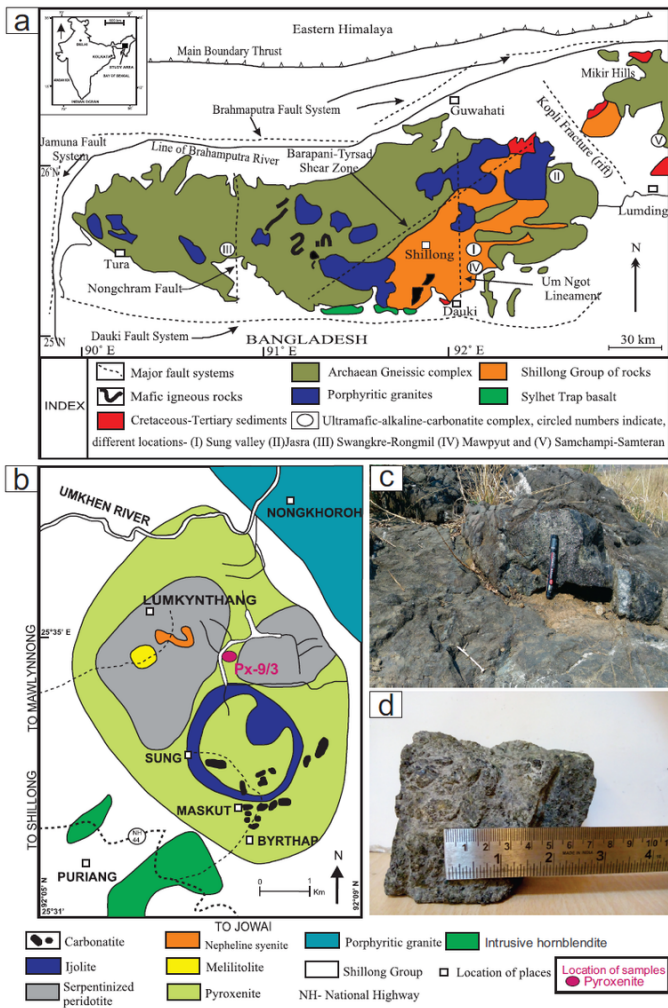


Figure 1

Geological maps, outcrop, and hand specimen. **(a)** Geological map of Shillong plateau. **(b)** Geological map of Sung valley, Meghalaya. **(c)** An outcrop of pyroxenite from Sung Valley, Meghalaya. **(d)** Section of a hand specimen of pyroxenite sample, no. Px-9/3.

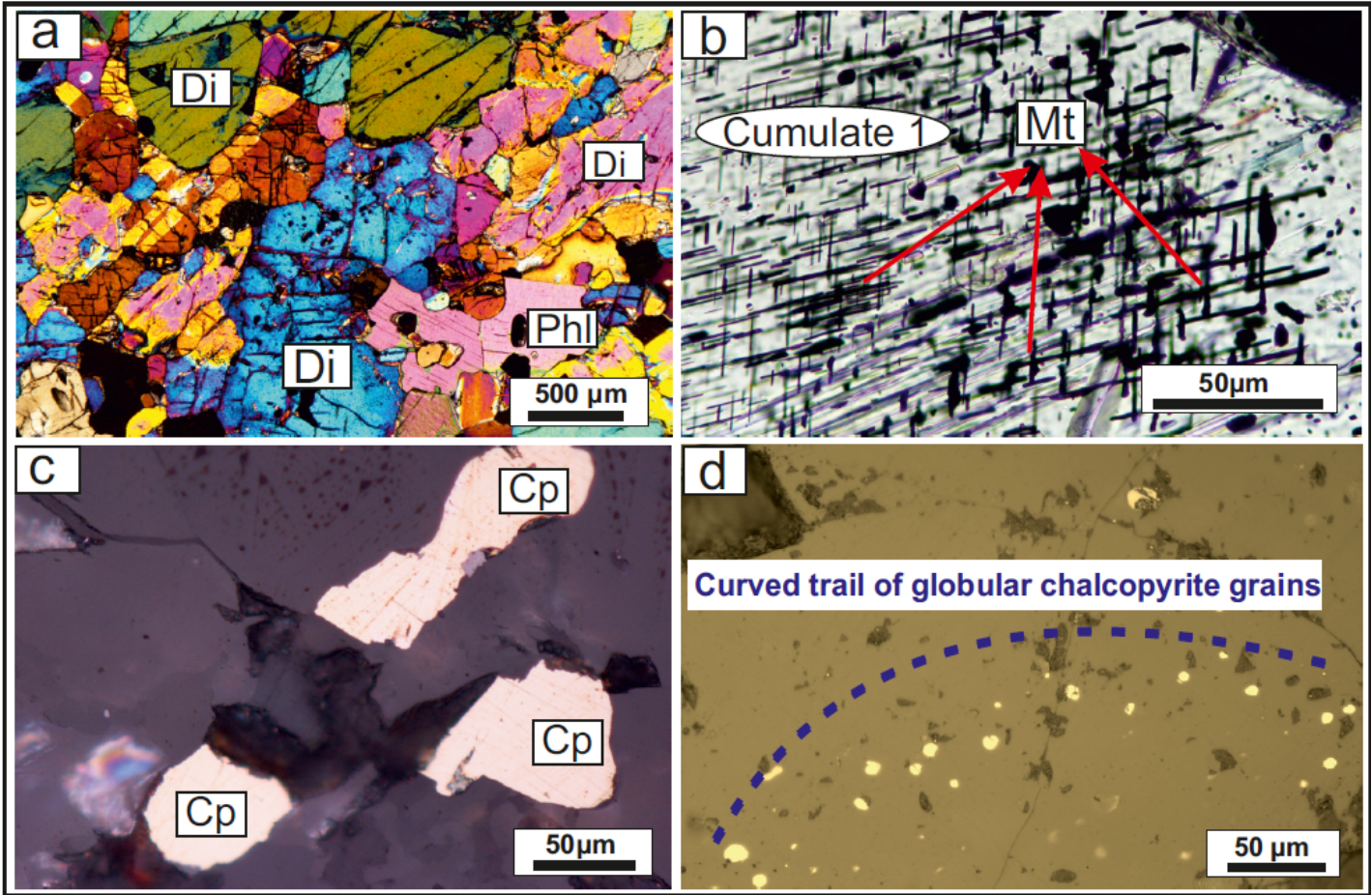


Figure 2

Photomicrographs showing petrographic features and mineral inclusions. (a) Cross-polarized photomicrograph showing different mineral phases in the pyroxenite. (b) Plane-polarized photomicrograph showing two set exsolution lamellae of magnetite oriented nearly at right angle in cumulate 1 Cpx. (c) Reflected light photomicrograph showing the presence of accessory sulfide minerals (chalcopyrite). (d) Reflected light photomicrograph showing curved trail of globular chalcopyrite inclusions. Di-diopside, Phl- phlogopite, Mt- magnetite, Cp-chalcopyrite.

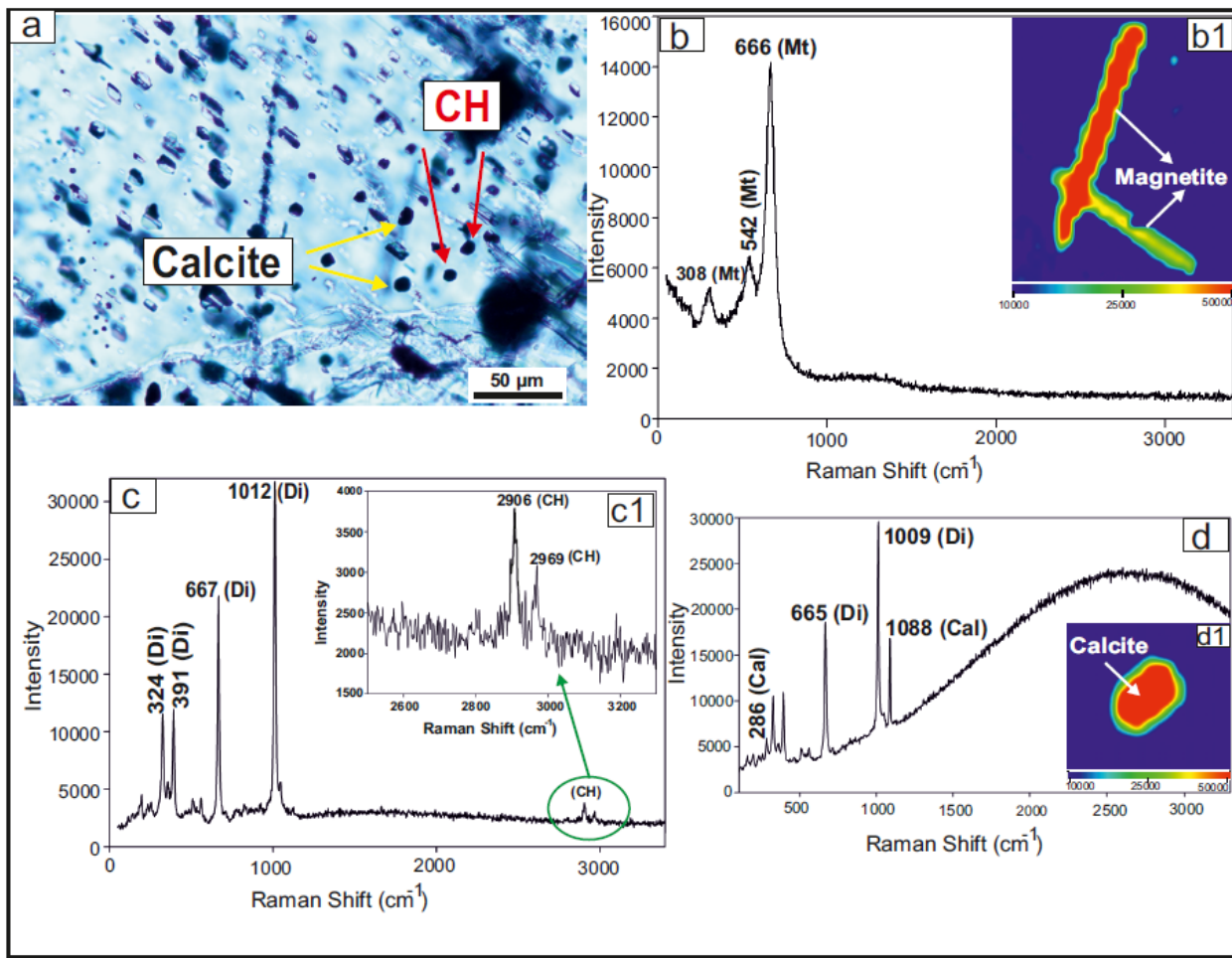


Figure 3

Raman spectra of inclusions in cumulate 1 Cpx. **(a)** Plane-polarized photomicrograph of primary inclusions of calcite and CH fluid within cumulate 1 Cpx grain. **(b)** Raman spectrum of magnetite exsolution needles; (Mt) showing strong bands at 542 and 666 cm^{-1} . **b1**: Inset: mapping of exsolution needles from Fig. 1b; along the XY direction showing magnetite. **(c)** Raman spectrum with the bands of CH at 2906 and 2969 cm^{-1} . **c1**: Inset: extracted Raman spectrum of CH. **(d)** Raman spectrum with the bands of calcite at 286 and 1088 cm^{-1} . **d1**: Inset: mapping along the XY direction showing the presence of calcite. Red-green blue colors in Figs. b1 and d1, are assigned to the distribution of major peaks of magnetite at 666 cm^{-1} and calcite at 1088 cm^{-1} respectively.

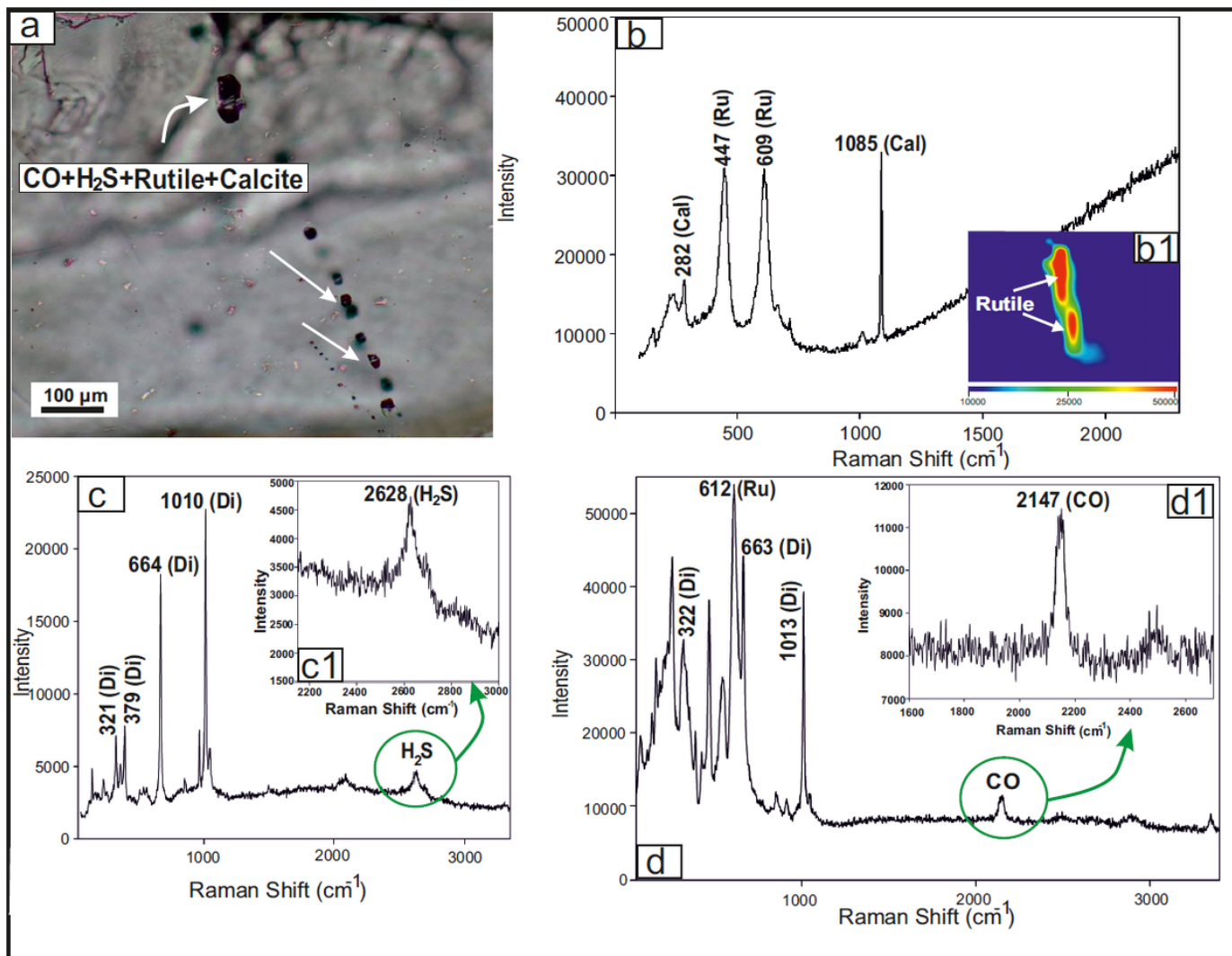


Figure 4
 Raman spectra of inclusions in cumulate 2 Cpx. **(a)** Plane-polarized photomicrograph of polyphase pseudo-secondary fluid inclusions trail in cumulate 2 Cpx. **(b)** Raman spectrum showing bands of rutile at 447 and 609 cm^{-1} and bands of calcite at 282 and 1085 cm^{-1} . **b1**: Inset: mapping along the XY direction of the analyzed spots showing the presence of rutile. Red-green blue colors are assigned to the distribution of major peak of rutile at 609 cm^{-1} . **(c)** Raman spectrum showing band of H_2S at 2628 cm^{-1} . **c1**: Inset: extracted Raman spectrum of H_2S . **(d)** Raman spectrum with the band of CO at 2147 cm^{-1} . **d1**: Inset: extracted Raman spectrum of CO.

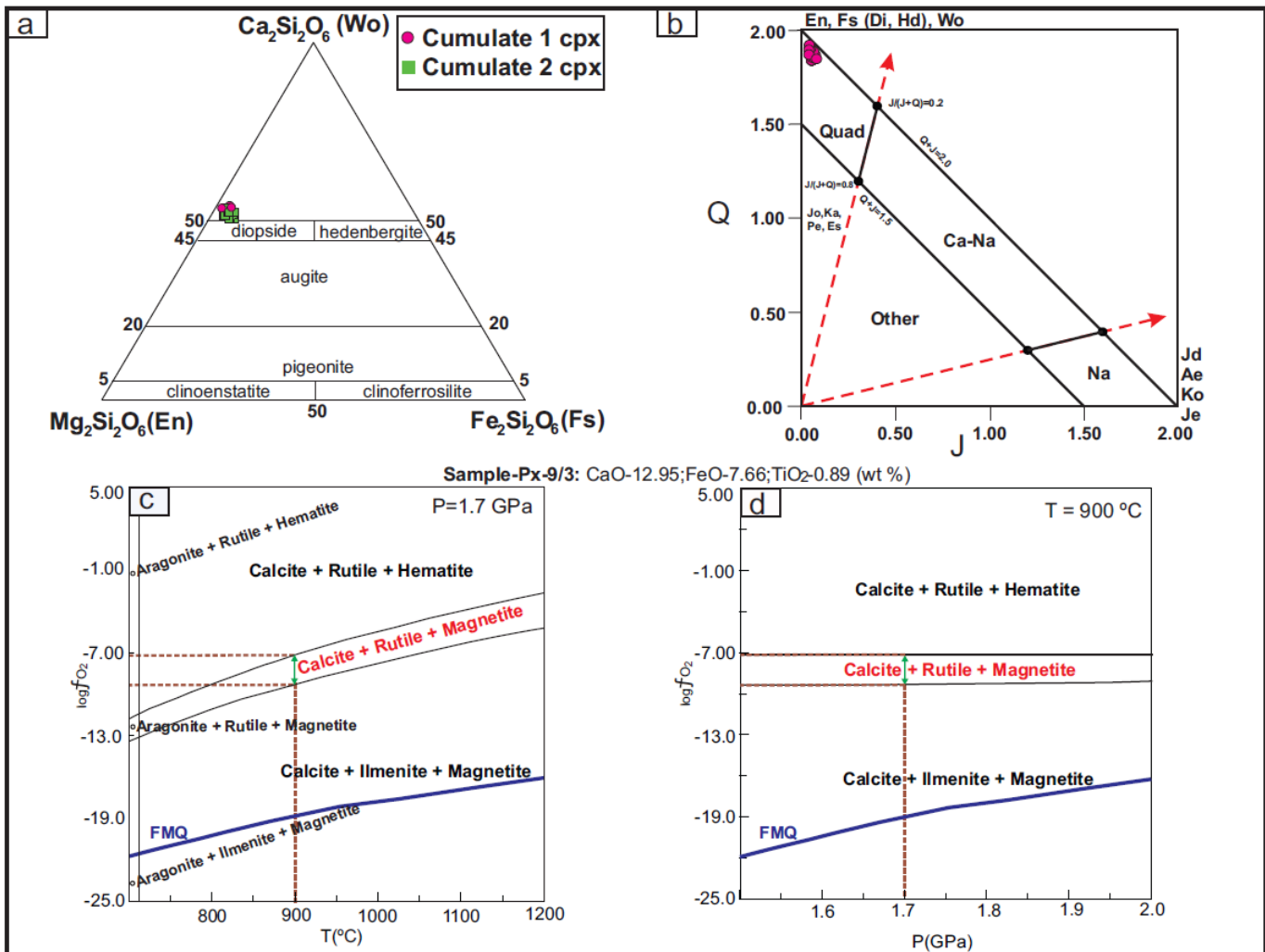


Figure 5

Plots related to mineral chemistry and oxygen fugacity calculation. **(a)** Triangular Ca-Mg-Fe classification diagram confirms that all points of mineral chemistry fall in the area close to diopside. **(b)** Q-J classification diagram for the pyroxenes (Morimoto et al., 1988, calculated by Winpyrox program, Yavuz, 2013). **(c)** The calculated T-fO₂ phase diagram in the CaO-TiO₂-FeO-O₂-CO₂ system at 1.7 GPa. **(d)** The calculated P-fO₂ phase diagram in the CaO-TiO₂-FeO-O₂-CO₂ system at 900 °C. The phase relations in Fig. 5c, d; were calculated using the Perplex 6.7.8 program (versions June 6th 2017, Connolly, 2009³⁸) and the internally consistent thermodynamic dataset of Holland and Powell (2001)³⁹.

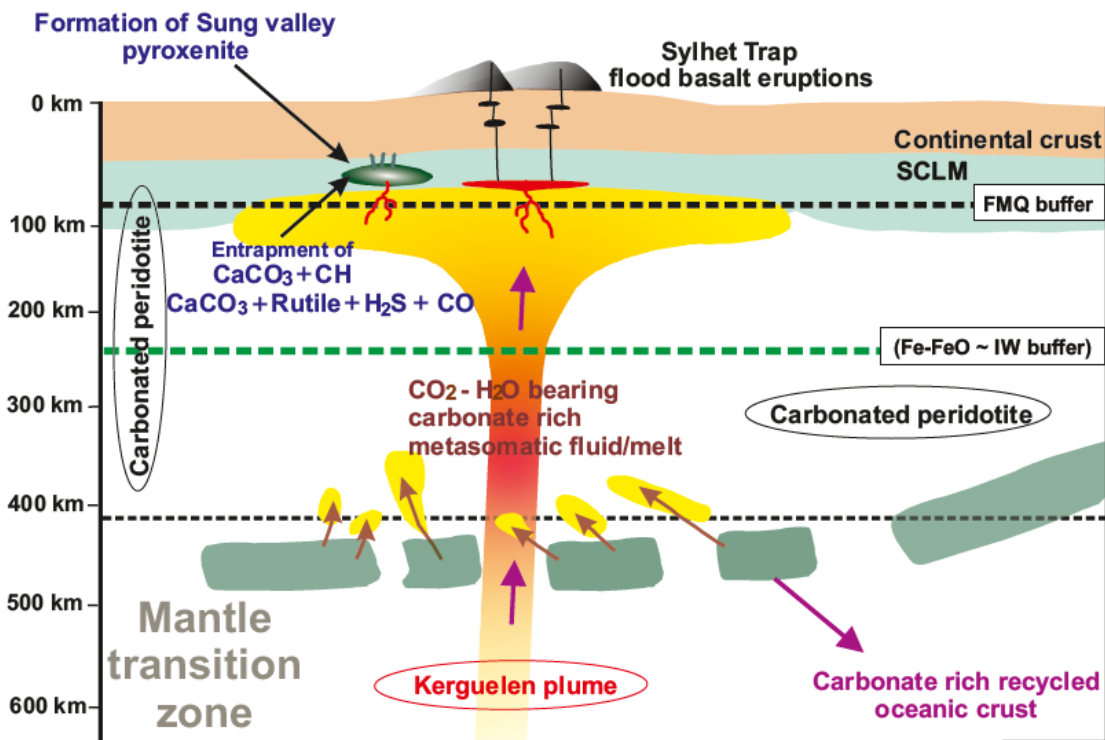


Figure 6

Schematic model illustrating the ascent of $\text{CO}_2\text{-H}_2\text{O}$ bearing carbonatitic melt and subsequent speciation of $\text{CO}_2\text{-H}_2\text{O}$ volatiles through formation of magnetite and rutile. Stage (1) carbon and sulfur-bearing phases in mantle are either primordial or sourced from subduction of carbonate rich oceanic crust and sediments into the mantle transition zone. Subsequent partial melting of slab gave rise to $\text{CO}_2\text{-H}_2\text{O}$ bearing carbonatitic melts. Stage (2) Carbonate melt metasomatizes the mantle peridotite to carbonated peridotite. The primary silicate magma generated through decompression/redox melting of carbonated peridotite incorporated in the Kerguelen plume. Stage (3) Interaction of pyroxenitic magma with $\text{CO}_2\text{-H}_2\text{O}$ fluids to form calcite and speciation of these $\text{CO}_2\text{-H}_2\text{O}$ volatiles to CH and CO in the presence of H_2S .

Supplementary Files

This is a list of supplementary files associated with this preprint. Click to download.

- [Supplementarymaterial.pdf](#)